

The open ocean kinetic energy cascade is strongest in late winter and spring

René Schubert^{1,*}, Oscar Vergara², and Jonathan Gula^{1,3}

¹University of Brest, CNRS, IRD, Ifremer, Laboratoire d’Océanographie Physique et Spatiale (LOPS), IUEM, Brest, France

²Collecte Localisation Satellites (CLS), Ramonville Saint-Agne, France

³Institut Universitaire de France (IUF), France

*corresponding author, rene.schubert@univ-brest.fr

Abstract

The oceanic kinetic energy cascade, the flux of kinetic energy between currents of different horizontal scales, shapes the structure of the global ocean circulation and the associated heat, salt, nutrient, and oxygen fluxes. Here, we show with a numerical ocean simulation that the surface geostrophic cascade can be estimated from satellite altimetry observations and present its regional distribution and seasonal cycle at scales of 40 to 150 km for large parts of the global ocean based on observations. The time-mean cascade is inverse (towards larger scales), strongest in large-scale current systems, and decreases with distance from these systems. In the open ocean, the inverse cascade is associated with a maximum in late winter at the smallest scales studied, which transitions to scales larger than 100 km within two to three months, consistent with the widespread absorption of mixed-layer eddies in spring.

1 Introduction

Ocean motions can be decomposed into movements at different horizontal scales ranging from large-scales ($\mathcal{O}(1000 \text{ km})$) through mesoscales ($\mathcal{O}(100 \text{ km})$) and submesoscales ($\mathcal{O}(100 \text{ m}) - \mathcal{O}(10 \text{ km})$) to microscales ($<\mathcal{O}(100 \text{ m})$). The flux of kinetic energy (KE) between ocean currents at different scales, the KE cascade, plays a key role in several aspects of global climate. First, in combination with the transformation of KE into available potential energy (and vice versa), the cascade mediates the balance between the oceans forcing by the atmosphere, primarily by wind at large scales, and the dissipation of KE into heat at molecular scales¹. Second, the KE cascade controls the scale-distribution of KE including the strength of the subtropical gyre², the strength and position of large-scale currents such as the Gulf Stream^{3,4}, the strength of inter-ocean exchanges such as Agulhas leakage⁵, and the strength and distribution of ocean mesoscale eddies^{6–8} and thus the associated transports of heat, salt, nutrients, and oxygen. Third, through ocean-atmosphere interactions, the ocean and atmosphere KE cascades determine their response times to external forcing⁹. This induces a modulation of the atmospheric circulation by the oceanic KE cascade. In addition to being a key component of the climate system, understanding the KE cascade is critical for the validation and development of climate models, particularly regarding the parameterization of the sub-grid-scale energetic fluxes and dissipation.

For the large mesoscales, the KE flux was computed from gridded sea-surface height data that were interpolated from along-track satellite altimetry measurements on a regular 0.25° and daily grid (AVISO) assuming geostrophy and an f-plane^{6,10–12}. The results showed an inverse cascade (from smaller to larger scales) at scales larger than about 75 km and a forward cascade (from larger to smaller scales) at smaller scales. While the forward cascade was later found to be an artifact of the filtering and interpolation technique onto the regular grid, the inverse cascade at larger scales was found to be robust to filtering^{11,12}. At scales of the maximum inverse flux (about 200 km), the cascade has been shown to be orders of magnitude smaller in the open ocean compared to regions of strong current systems¹³. This is not surprising, as the inverse cascade is stopped at smaller scales in the open ocean, for example due to the Rhines effect¹⁴. Substantial inverse fluxes occur at these scales only in the large-scale current systems, where very large mesoscale eddies form as a consequence of large-scale instabilities and interact with the large-scale currents. Regional submesoscale-permitting simulations and regional observations have shown that the inverse cascade extends into the submesoscales to scales of the mixed-layer Rossby radius of deformation (about 15 km)^{12,15–20}. Applying a filtering approach for computing the KE flux^{21–24} to submesoscale-permitting model data, it was found that the underlying process of the submesoscale inverse cascade is primarily the absorption of submesoscale mixed layer eddies by mesoscales eddies¹⁷. Consistently, the maximum of the submesoscale inverse flux has been found to occur immediately after the submesoscale season in late winter and to shift to larger scales in spring¹⁷. Based on observations, the existence of the submesoscale inverse KE cascade and its seasonality could only be demonstrated for small ocean regions^{16,18–20}. Indirect evidence that this submesoscale inverse cascade is active in large parts of the global ocean has recently been provided by

50 high-resolution satellite products²⁵. Recent model studies have applied Helmholtz decomposition and principal strain coordinate
 51 transformation prior to the computation of the scale KE flux, and have shown that the inverse cascade is primarily driven by
 52 geostrophically balanced flows^{26,27}. This confirms that it should be possible to analyze the near-surface inverse KE cascade on
 53 the basis of sea-surface height.

54
 55 In this study, we provide an observation-based estimate of the surface geostrophic KE cascade and its seasonal cycle at
 56 scales of 40-150 km in large parts of the global ocean. We use information on the dynamics in the respective scale-band from
 57 satellite along-track altimetry data measured by JASON-3 as well as from a submesoscale-permitting simulation of the Atlantic.
 58 The KE flux can not be computed directly from along-track sea-surface height. However, using the simulation, we prove that it
 59 is possible to estimate the KE flux from the simulated sea-surface height along the tracks of JASON-3 and apply the proposed
 60 estimation technique to the actual measurements.

61 2 Results

62 If the measured along-track absolute dynamic topography (η) is dominated by geostrophic flows, the across-track f-plane
 63 geostrophic flow component can be computed as $u = -\frac{g}{f}\eta_y$, where $g = 9.81 \text{ m s}^{-2}$ is the gravitational acceleration, $f =$
 64 $2\Omega \sin(2\pi \frac{\theta}{360^\circ})$ is the Coriolis parameter with the Earth's angular speed $\Omega = \frac{2\pi}{86400} \text{ s}^{-1}$ and the latitude θ , and y is the along-track
 65 direction with increasing latitude. Partial derivatives of a with respect to b are written here and in the following as $\frac{\partial a}{\partial b} = a_b$. For
 66 this study, we use five years of tide-corrected and filtered measurements of η taken by the JASON-3 satellite along the tracks
 67 shown in Figure 1a. From these, we estimate the surface geostrophic $5^\circ \times 5^\circ$ domain-averaged scale-KE flux through a specific
 68 scale L as

$$\langle \Pi_{est} \rangle = -C(L)\rho_0 \overline{\langle u^2 \rangle - \overline{uu}} \langle |\bar{u}_y| \rangle, \quad (1)$$

69 where angle brackets indicate averages over $5^\circ \times 5^\circ$ subdomains for each measurement cycle, C is an estimation coefficient
 70 identified from a numerical ocean simulation, and $\rho_0 = 1024 \text{ kg m}^{-3}$ is the standard density. The overlines denote fields
 71 convoluted with a tophead kernel whose length is equal to that of the respective scale L and which is normalized so that it
 72 integrates to 1. The computation of C and the proof that the proposed estimation works is given in section 3.

73
 74 If η is not dominated by geostrophic flows, the computation of geostrophic currents from the measurements fails. A lower
 75 bound for the scales at which the respective gradients of η can be used to derive geostrophic flows is provided by the transition
 76 scale from balanced to unbalanced flows T . T is estimated from the JASON-3 along-track data with a previously published
 77 method²⁸ and is averaged over the same $5^\circ \times 5^\circ$ grid on which we estimate the scale KE flux. T is associated with lower
 78 values in regions with strong balanced flows (large-scale currents and surface eddy pathways) and higher values in regions with
 79 weak balanced flows (weak eddy activity)²⁸. Furthermore, T is associated with a seasonal cycle, with lower values in spring
 80 when there are more balanced submesoscale vortices, and higher values in summer and autumn when the surface signature
 81 of internal waves is amplified²⁹. In Figures 1 and 2 we highlight with black lines the regions, scales and seasons where the
 82 results are partially corrupted by too strong imprints of unbalanced flows into the absolute dynamic topography measurements.
 83 Furthermore, we exclude the tropics between $15^\circ S$ and $15^\circ N$ from our analysis, because the baroclinic mode-1 and mode-2
 84 diurnal tides significantly affect the SSH-spectrum³⁰ there, and consequently T exceeds 75 km throughout the year³¹.

85 2.1 The time-mean scale KE flux

86 The time-mean estimated fluxes at scales of 60, 140 and 200 km are shown in Figure 1. The largest (inverse) fluxes occur at all
 87 scales in regions of very strong near-surface current systems, such as the Gulf-Stream - North-Atlantic-Current system, the
 88 Agulhas system, the Brazil-Malvinas-Confluence or the Kuroshio. The further away from the large-scale currents, the smaller
 89 the fluxes. Fluxes at 140 km and 200 km scales are very close to each other and have substantial amplitudes almost only in
 90 regions of large-scale current systems. At 200 km, the pattern is very similar to the one presented in a previous study based on
 91 gridded AVISO data¹³. At this scale, almost no time-mean fluxes are found in the open ocean. At 60 km, fluxes of about 10-20
 92 mW km⁻¹ m⁻³ occur in large parts of the mid-latitudes. This is consistent with wide-spread mixed-layer instabilities leading
 93 to the formation of submesoscale eddies, which are subsequently absorbed by the mesoscales¹⁷.

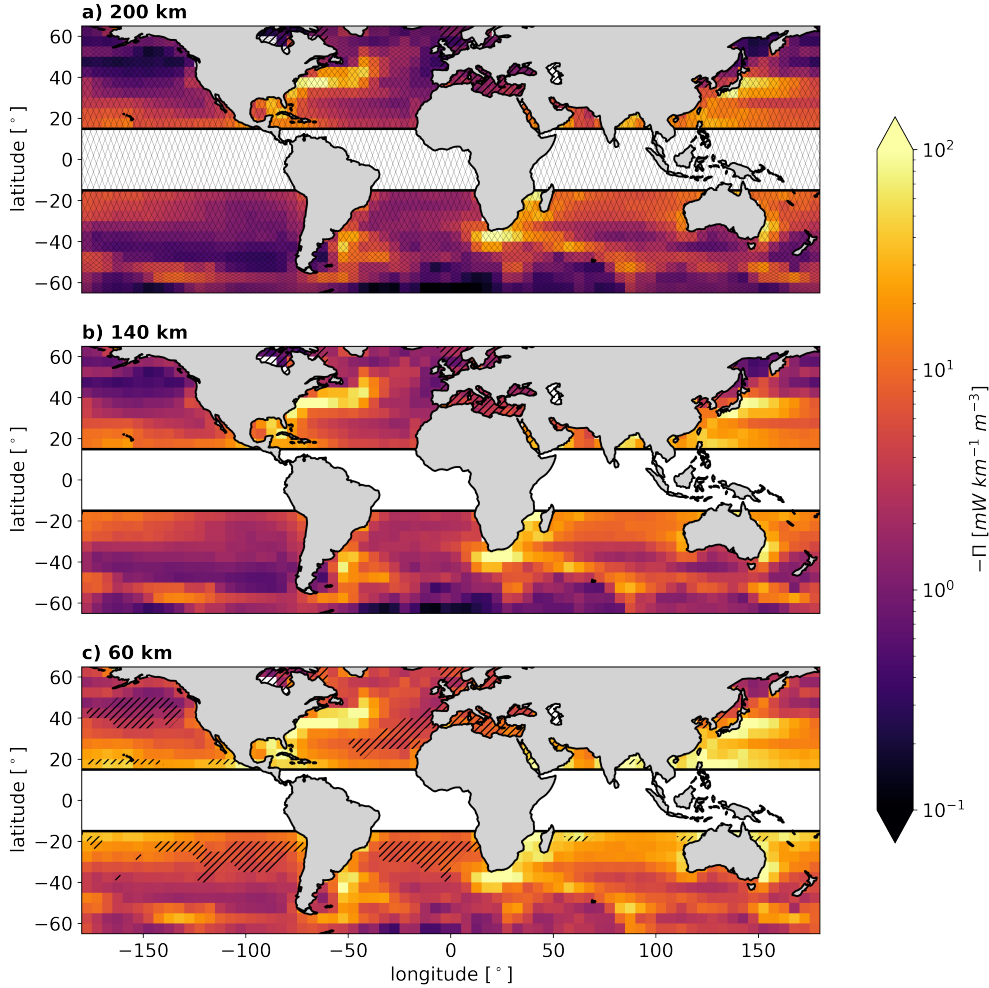


Figure 1. The time-mean inverse scale kinetic energy flux The time-mean inverse scale kinetic energy flux $-\Pi_{est}$ from JASON-3 SSH at scales of 200 km (a), 140 km (b), and 60 km (c). In a), thin black lines show the JASON-3 tracks. Hatches mark regions where the time-mean transition scale from balanced to unbalanced flows T is larger than the scale, $-\Pi_{est}$ is shown for, and thus, where the results have to be interpreted with care.

2.2 The seasonal cycle of the scale KE flux

The seasonal cycle of Π_{est} and its scale-distribution are shown in Figure 2. At 60 km, the anomalies of the FMA-mean (Fig. 2a) and the ASO-mean (Fig. 2b) relative to the 2017-2021 mean flux show enhanced inverse fluxes in spring and reduced inverse fluxes in autumn for most open ocean regions. This is consistent with a previously published map of the seasonal difference in geostrophic KE computed from along-track altimetry²⁵. In the open ocean, enhanced fluxes occur in winter and spring with a maximum in early spring (February in the Northern Hemisphere and July in the Southern Hemisphere) at 40 km scale (Fig. 2c and 2d). During the following three to four months, enhanced fluxes occur at increasingly larger scales. Deeper mixed layer depths in winter allow for the accumulation of more available potential energy at mixed-layer fronts. Mixed-layer baroclinic instability of the fronts releases this potential energy into KE in the form of mixed-layer eddies²⁵. These eddies have a diameter on the order of the mixed-layer Rossby deformation radius (about 15 km) and are stronger and more frequent in winter. Subsequently, these eddies grow and are absorbed by mesoscale eddies. The absorption process takes about 2-3 months, resulting in a shift of the maximum scale KE flux from late winter at 30 km to late spring at 140 km. This climatological scale-time pattern of the observation-based estimated inverse flux is consistent with that of the power-spectral density of KE computed from AVISO³² and along-track altimetry²⁵. The same consistency was also found in a simulation of the open ocean near the Agulhas-system¹⁷. In regions of strong large-scale flows, in particular the Gulf Stream and Kuroshio extensions, the Brazil Malvinas Confluence, and the Agulhas region and Return Current, the estimated fluxes at 60 km mainly show an opposite seasonal cycle to that of the open ocean. This is consistent with results from a recent model study of the Gulf Stream, which

111 found a stronger seasonal cycle of the balanced cascade outside of the Gulf Stream core, including a scale-shift of the maximum
 112 inverse flux and a reduced seasonality without a scale-shift of the maximum in a region that partially includes the Gulf Stream²⁶.
 113 Furthermore this is consistent with previously published results on along-track altimetry based geostrophic KE levels, which
 114 revealed an opposite seasonal cycle within the strong current-systems²⁵. We speculate that the reason for this phenomenon is
 115 that other energetic submesoscale and mesoscale processes overcome the seasonal cycle of mixed-layer instabilities and the
 116 subsequent inverse cascade of the resulting mixed layer eddies. In the future, these other processes need to be identified.

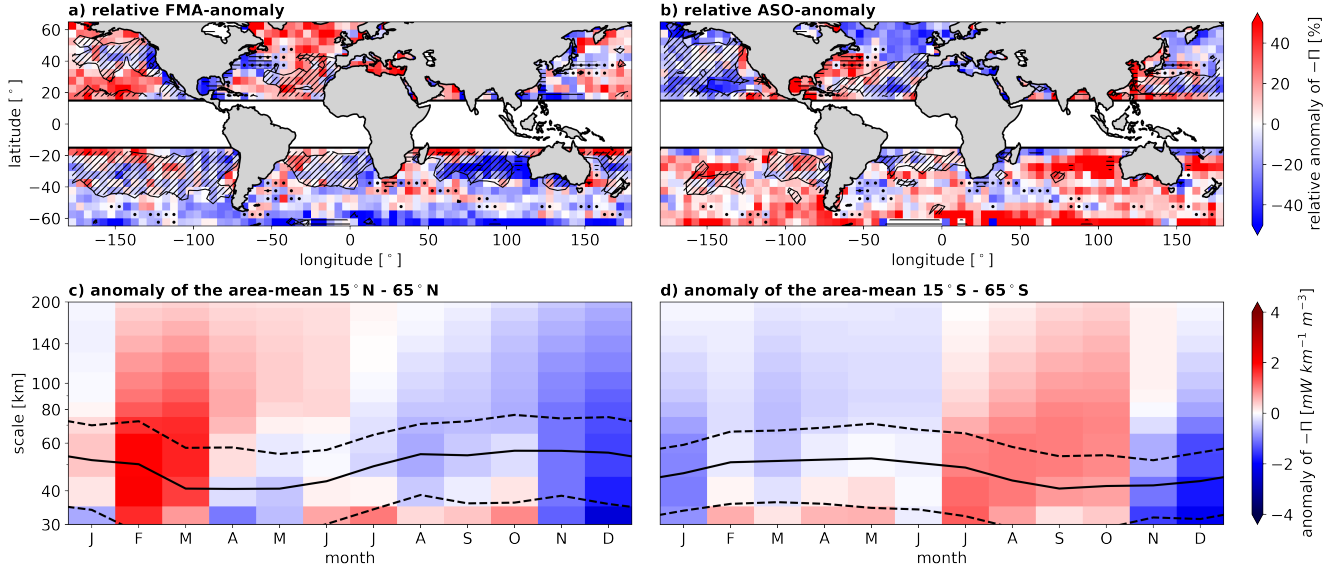


Figure 2. The seasonal cycle of the inverse scale kinetic energy flux Monthly climatological anomalies of the scale kinetic energy flux $-\Pi_{est}$ from JASON-3 with respect to the 2017-2021 mean. Red (blue) colors mark enhanced (reduced) inverse cascade. Shown are the relative anomalies for the FMA-mean (**a**) and ASO-mean (**b**) flux at 60 km, as well as the anomalies for the area-mean flux between 15°N and 65°N (**c**), and between 15°S and 65°S (**d**). Contour lines and diagonal hatches mark where the maximum transition scale from balanced to unbalanced flows T is in the respective season larger than 60 km and thus, where the results are potentially erroneous due to non-geostrophic gradients of η . Regions of strong large-scale currents are excluded before the area-averaging for the bottom panels. They are identified by the temporal standard deviations of 2017-2021 AVISO-SSH averaged over $5^{\circ} \times 5^{\circ}$ domains larger than 20 cm (dotted) and by anomalies of the KE flux that are larger than $15 \text{ mW km}^{-1} \text{ m}^{-3}$ at 60 km (horizontal hatches). The respective area-mean T (solid line) plus and minus one standard deviation (dashed lines) are shown in **c** and **d**.

117 Particularly in summer, in regions of weak mesoscale activity at scales of 70 km and smaller, the measured absolute dynamic
 118 topography is not dominated by balanced flows and $-\Pi_{est}$ gives spuriously enhanced values. This manifests itself in a spurious
 119 reduction or reversal of the seasonal cycle at 60 km in regions such as the North East Pacific or the Central Atlantic, where the
 120 maximum T of the respective season is larger than 60 km (contours and hatches in Fig. 2a and 2b), as well as small secondary
 121 maxima of $-\Pi_{est}$ in summer (August in the Northern Hemisphere and February in the Southern Hemisphere) mainly at scales
 122 smaller than 70 km (Fig. 2c and 2d).

123 3 Methods

124 3.1 JASON-3 satellite along-track altimetry data

125 JASON-3 measures the absolute dynamic topography η , the sum of the sea-level anomaly and the mean dynamic topography,
 126 between 66°S and 66°N with an along-track resolution of about 6 km at 1 Hz and a repeated measurement of each track every
 127 10th day. Below scales of 25-35 km, JASON-class data are associated with noise^{33,34}. This noise is associated with a seasonal
 128 cycle that is similar, but not identical, to that of the submesoscale KE level³⁴ (at least north of 40°S ³⁵): higher noise and
 129 submesoscale KE in winter and lower in summer. The sea-level anomaly is available in an original (unfiltered) and a low-pass
 130 "filtered" version. Fourier-analysis shows that the seasonal cycle of power spectral density of the unfiltered η has deviations
 131 from 20 km on all scales larger than 30 km (Fig. 3e), indicating that the seasonal cycle at these scales is not corrupted by
 132 measurement noise. Furthermore, for this study, we use the tide-corrected data, where the barotropic tides and the coherent part
 133 of the baroclinic tides for modes M2, K1, O1 and S2 have been removed from the data. Note, however, that there is a residual

134 effect of tides that cannot be corrected. Note also that η is the sea-surface height (SSH) corrected by the geoid. Since the geoid
135 is associated with very large scales, this correction is not relevant for the analysis presented in this study. Therefore, η is also
136 referred to as SSH in the following.

137 **3.2 GIGATL1 simulation**

138 The GIGATL1 simulation³⁶ used here has been performed with the Coastal and Regional Ocean CCommunity model (CROCO,
139 10.5281/zenodo.7415055), which is based on the Regional Ocean Modeling System (ROMS³⁷). The integration is performed
140 on an Arakawa C-grid³⁸ using 100 vertical terrain-following sigma-levels where the bathymetry is taken from the SRTM30plus
141 dataset. Vertical mixing is parameterized with the k-epsilon turbulence closure scheme with applied Canuto A stability function.
142 No explicit lateral diffusivities and viscosities are used. The effect of bottom friction is parameterized with a logarithmic law
143 using a roughness length of 0.01 m. The GIGATL1 grid is orthogonal based on an oblique Mercator projection and designed
144 to have nearly uniform spacing in both horizontal dimensions. The grid spacing varies from 1 km at the central longitude
145 of the grid to 735 m at the west and east extremes of the grid. A simulation with a grid-spacing three times as large as the
146 one of GIGATL1, "GIGATL3", has been initialized in January 2004. Initialization fields and boundary conditions are from
147 Simple Ocean Data Assimilation (SODA³⁹). GIGATL1 is initialized from the restarts of GIGATL3 in July 2007 and integrated
148 twice, one experiment with simulated tides and one experiment without simulated tides. All simulations are forced by hourly
149 atmospheric forcing data from the Climate Forecast System Reanalysis (CFSR) with a bulk formulation and a stress correction
150 approach to parameterize the surface ocean current feedback to the atmosphere⁴⁰. Barotropic tidal forcing at the boundaries
151 and tidal potential and self attraction from TPXO7.2 and GOT99.2b are applied to GIGATL3 and GIGATL1 with tides. In this
152 study, we analyze snapshots every fifth day over the period April 2008 to March 2009 for both simulations.

153 **3.3 Model Validation**

154 The temporal standard deviation of SSH, computed from daily averages during Apr 2008 - Mar 2009 averaged onto the AVISO
155 grid, shows similar large-scale patterns for GIGATL1 without simulated tides and AVISO (Fig. 3a and 3b). The largest values
156 occur in the region of the Gulf Stream, North Atlantic Current and Brazil Malvinas Confluence systems, moderate values in
157 the surrounding ocean, as well as in the Agulhas ring path, the Azores Current, and the North Equatorial Counter Current,
158 and low values above the shelves and in the central subtropical gyres. The simulated SSH variabilities are smaller than in the
159 observations in the Gulf Stream extension, the Brazil Current extension, and the Agulhas Ring Path, and larger north of 50°N.
160 The standard deviation of SSH in the Northwest-Corner and the North Atlantic Current are in remarkably good agreement.
161 The too low simulated SSH variability in the Agulhas ring path is a result of the monthly boundary conditions applied at the
162 southern boundary of the domain, which are not frequent enough to resolve the full variability of the energetic eddies drifting
163 out of the Agulhas region into the Atlantic.

164 Time-mean horizontal wavenumber spectra computed from SSH at JASON-3 tracks in a $20^\circ \times 20^\circ$ domain in the open
165 ocean show similar results for JASON-3 and GIGATL1 without simulated tides (Fig. 3c). For comparison, the GIGATL1 SSH
166 is extracted at the measurement locations of JASON-3 from model snapshots every fifth day. The SSH-spectra from GIGATL1
167 without tides and the unfiltered, tide-corrected JASON-3 data show a very good agreement at scales larger than 60 km. At scales
168 smaller than 60 km, the spectrum of the observations shows higher values compared to the simulation, which could be due to
169 observational noise or unresolved processes. The spectrum of the filtered JASON-3 SSH follows that of the unfiltered down to
170 45 km, but with a shallower slope between 60 km and 45 km than in the simulation, which shows a k^{-4} slope down to 30 km.

172 Hovmöller plots of the monthly climatology of the SSH-spectrum for both the simulation and the observations (Fig. 3d
173 and 3e) show maxima that shift from winter at scales of $\mathcal{O}(10 \text{ km})$ to summer at scales of $\mathcal{O}(100 \text{ km})$ similar to the maximum
174 inverse cascade estimated from JASON-3 (Fig. 2c). This shift is consistent with previous results from AVISO and simulations^{17,32}, as well as with a maximum of submesoscale activity in winter and spring and a subsequent inverse cascade involving
175 the growth of submesoscale eddies and their absorption by mesoscale eddies¹⁷. For the simulation, the Hovmöller plot is more
176 patchy and shows the shift to larger scales one to two months later than in the observations. This can be due to the specific
177 conditions in the single simulated year, which is compared here to a five-year average from the observations.

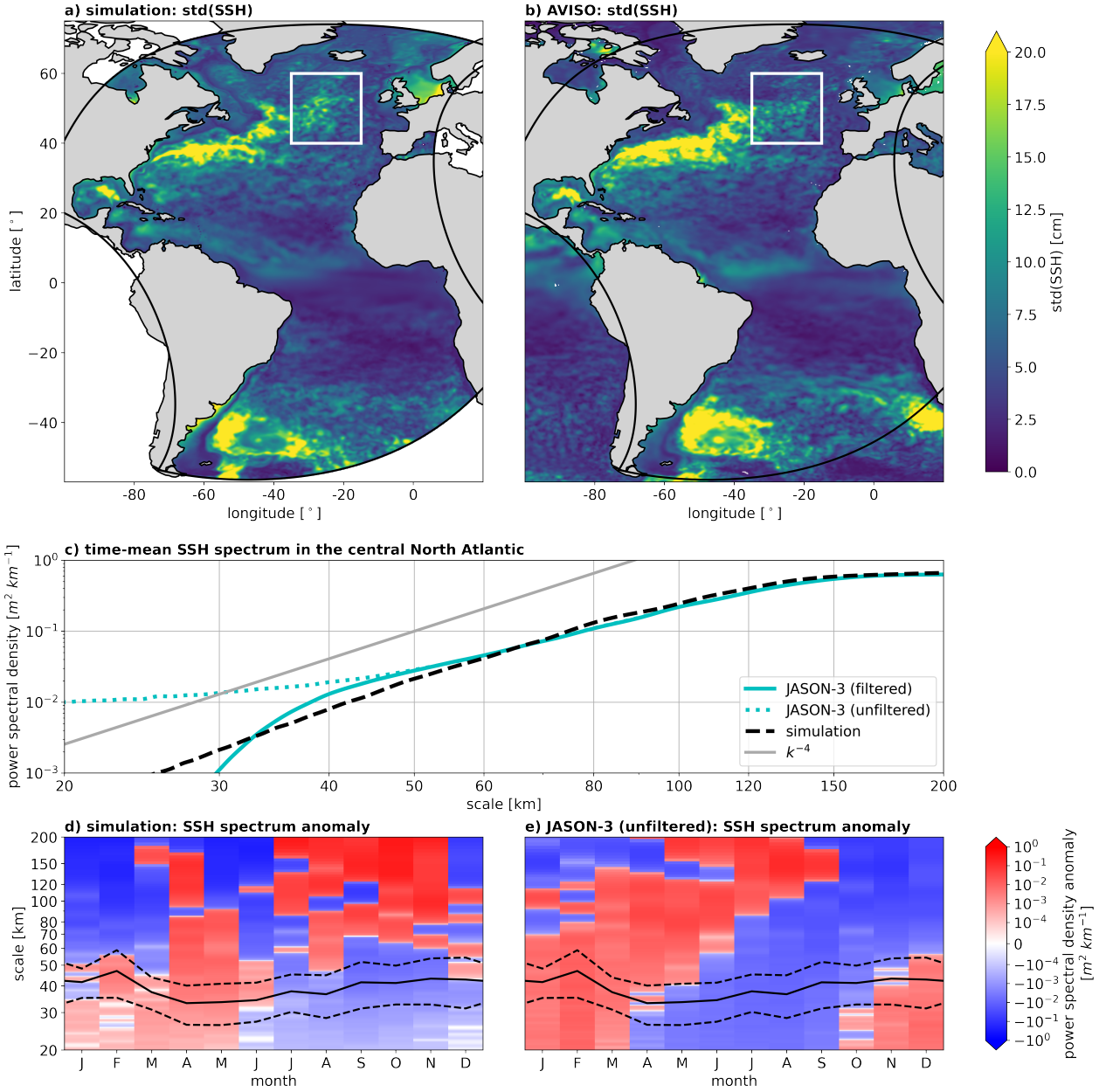


Figure 3. Model Validation The standard deviation of SSH computed from Apr 2008 - Mar 2009 daily mean fields of GIGATL1 without simulated tides (**a**) and AVISO (**b**). Thick black lines show the GIGATL1 domain, and the white box the region for which the Fourier-transform is performed for the middle and bottom panels. **c**) shows the time-mean SSH spectra and a gray straight line for the k^{-4} slope. **d**) and **e**) show Hovmöller plots of the monthly climatological anomalies of the SSH spectra with respect to the mean over the period Apr 2008 - Mar 2009 for **d**) and 2017-2021 for **e**). The respective area-mean T (solid line) plus and minus one standard deviation (dashed lines) are shown in **d**) and **e**).

180 3.4 The scale KE flux

181 With the filtering approach, the scale KE flux can be computed as

$$\Pi = -\rho_0 [(\bar{u}^2 - \bar{u}^2)\bar{u}_x + (\bar{u}\bar{v} - \bar{u}\bar{v})(\bar{u}_y + \bar{v}_x) + (\bar{v}^2 - \bar{v}^2)\bar{v}_y], \quad (2)$$

182 where u and v are the total horizontal velocity components in perpendicular directions x and y ²¹⁻²⁴. The overlines denote fields
183 convolved with a two-dimensional top-head kernel whose diameter is equal to that of the respective scale L and which is
184 normalized by the respective enclosed area so that it integrates to 1. Π is only computed if the full kernel area is filled with data.

To reduce the memory requirement for convolutions in the computation of Π , which increases exponentially with the respective scale, u and v are first averaged within 5×5 grid-cell boxes. This has almost no effect on the results, as the variations of the simulated values on the near-grid-scale are very small. Due to limits in computational time and storage, the computations were only feasible for snapshots every fifth day. While this does not affect the results for area-averages, the results for time-averages may contain aliasing effects.

Large amplitudes of surface time-mean Π occur mainly in regions of strong current systems. While the Gulf Stream - North Atlantic Current and Brazil Malvinas Confluence systems show time-mean fluxes of both signs at 60 km scales, the equatorial current system is associated with a time-mean forward cascade (Fig. 4a). The area-mean flux for a large region in the North Atlantic, shows a dominant forward cascade in summer and autumn (JJASON) and a dominant inverse cascade in winter and spring (DJFMAM) (lower panel in Fig. 4a). The maximum inverse cascade shifts by a few months with increasing scale. This is consistent with the absorption of the winter-time submesoscale vortices by the mesoscales which takes this time¹⁷, and with the seasonal cycle of the SSH spectrum in the North Atlantic Current (Fig. 3d).

198
199

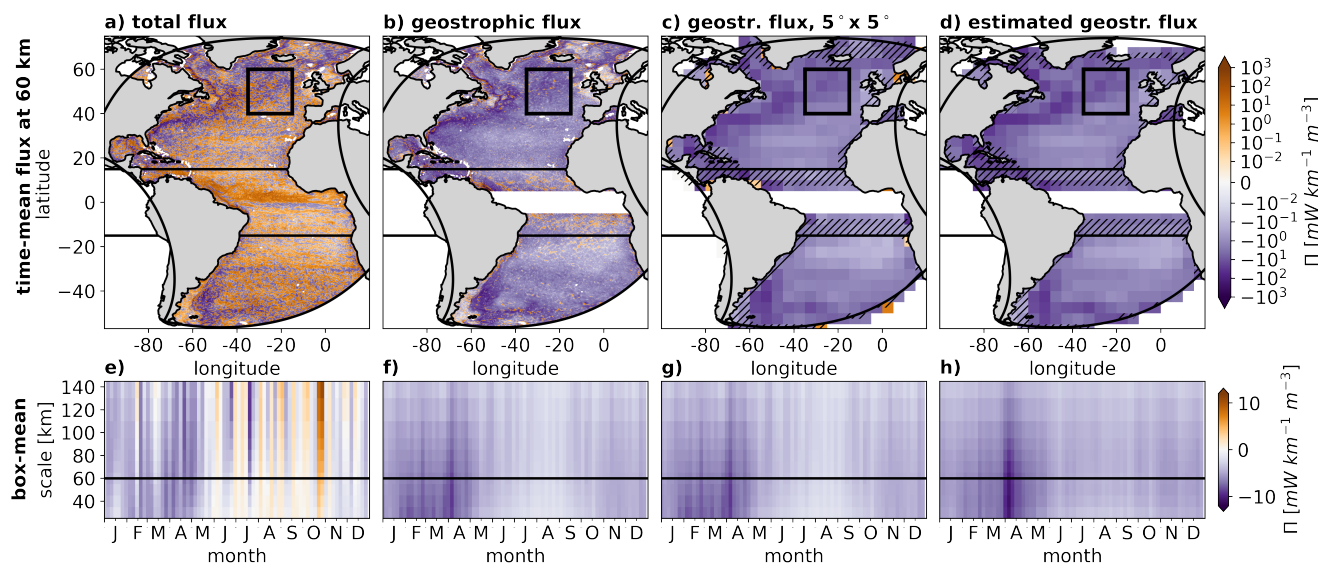


Figure 4. The simulated scale kinetic energy flux The scale kinetic energy flux Π computed from GIGATL1 without simulated tides in the period Apr 2008 - Mar 2009 from the total velocity (a), the geostrophic velocity (b), the geostrophic velocity and subsequently averaged over $5^\circ \times 5^\circ$ domains (c), and estimated with equation (1) from SSH cut from the simulation along JASON-3 tracks (d). The time-mean flux at 60 km scales is shown in a) to d). 15°S and 15°N are shown with black horizontal lines. Hatches mark regions that have been excluded for the computation of the estimation coefficient C . In e) to h), Hovmöller plots of the respective area-averaged flux in the North Atlantic are shown (domain marked with a black box in a) to d)). The scale of 60 km is marked with a black line.

The geostrophic scale KE flux can be computed by using (2), with the geostrophic velocity. Noisy large-amplitude time-mean geostrophic fluxes occur on the shelf, as well as in the tropics (Fig. 4b). Away from these regions, the time-mean geostrophic flux is inverse almost everywhere. When averaged over $5^\circ \times 5^\circ$ regions, the instantaneous geostrophic flux is only very rarely forward. In the time-mean, only a few regions near the coast or near the boundary of the domain show time-mean forward fluxes (Fig. 4c). Geostrophic fluxes averaged over the North Atlantic box show a dominant inverse cascade at all times and scales as well (bottom panels in Fig. 4b and 4c). The inverse cascade is maximum at the smallest investigated scales in February, March, and April, which shifts to April and May at scales of 100 km and larger. The similar timing and amplitude of the inverse cascade from the total velocity (Fig. 4a) support that balanced flows are primarily responsible for the inverse cascade, as shown in previous studies^{26,27}. Furthermore, this confirms that the near-surface winter and spring inverse cascade can be studied using SSH. However, for the interpretation of the geostrophic flux, one needs to be aware that the ageostrophic (net forward) cascade reduces the geostrophic (net inverse) cascade mainly at scales smaller than 40 km throughout the year (Fig. 4a). Note that the results presented here for the surface cascade from total velocities correspond to an extreme case, as forward fluxes are surface intensified and restricted to the very upper ocean, while the inverse cascade driven by the balanced flows extends deep into the

ocean^{17,27}. The estimate of the geostrophic flux presented in section 2 is therefore more representative of the cascade over the depth-range of surface intensified balanced flows than of the cascade directly at the surface.

3.5 Estimating the scale KE flux from along-track data

In order to access the smallest scales observed by satellite altimetry, we must use the non-gridded along-track SSH product. However, it is not possible to compute the geostrophic Π directly from along-track SSH, as one can only compute the across-track geostrophic velocity component. This implies that, of all the terms in (2), only the Leonard stress $\bar{u}^2 - \bar{u}^2$, and the along-track derivative \bar{u}_y are computable. For this study, we propose to estimate the flux with equation (1), which includes the product of these two terms giving the correct unit of a scale KE flux. Since $\bar{u}^2 - \bar{u}^2$ is always positive, using the absolute value of \bar{u}_y along with the minus sign means that the estimated geostrophic flux is globally inverse, consistent with what we found for the time- and area-averaged geostrophic fluxes in the simulations (Fig. 4c), with AVISO based observational studies at larger scales^{6,11}, and with theoretical studies that showed that the balanced flows are associated with inverse fluxes^{26,27}. However, in some shelf regions, $5^\circ \times 5^\circ$ averaged forward geostrophic fluxes do occur in our simulations, which implies that the estimated fluxes from JASON-3 need to be interpreted with care on the shelf. Trying to estimate the sign of the geostrophic flux directly, for example by using \bar{u}_y without taking its absolute value and removing the minus sign in equation (1), has not been successful.

We average both subterms in equation (1) over $5^\circ \times 5^\circ$ boxes, as the estimation works better the larger this region is, and as they are large enough to cover reasonable amounts of along-track data (which have a track-to-track distance of several degrees for ascending and descending tracks (Fig. 1a). This technique is associated with the inclusion of information from both horizontal directions, as the angle between ascending and descending tracks is large (Fig. 1a), and thus reduces the effect of the isotropy assumption that is necessarily made when one-dimensional data is cut from a two-dimensional field and then used to make a statement about that field.

The estimation coefficient C is identified from the simulations for each chosen scale by area- and time-averaging the term $\langle \Pi \rangle / (-\rho_0 \langle \tau_{uu} \rangle \langle |\bar{u}_y| \rangle)$, where $\langle \Pi \rangle$ is computed from the 5x5 grid-cell averaged SSH field and the divisor terms from the SSH extracted from the simulation along the JASON-3 tracks. For the final area-averaging of the term, regions near the coast and boundary of the simulation, where the respective $5^\circ \times 5^\circ$ domain includes only a small ocean area are excluded (shown hatched in Fig. 4c), as well as regions and times where $L < T$. For scales of [30,40,50,60,70,80,90,100,120,140,160,180,200] km, C is computed to be [0.32,0.26,0.23,0.22,0.20,0.19,0.18,0.17,0.15,0.14,0.13,0.12,0.11] and thus shows an exponential decay with larger scales. Computing C from a parallel simulation with simulated tides, gives similar values (see Supplementary Note 1 and Supplementary Figure 1).

Comparisons of the original and estimated time-mean fluxes at a scale of 60 km and their area-mean in the North Atlantic box show that the estimation reproduces the horizontal and temporal patterns and their amplitudes reasonably well (Fig. 4c and 4d). Large differences only show up in the Gulf Stream extension, where the flux is overestimated, and in a few shelf regions where the original flux is forward and thus cannot be estimated correctly with equation (1). The former may be due to the extreme non-isotropy of the core Gulf Stream extension and indicates that the fluxes are overestimated in similar energetic non-isotropic flows, such as the western Kuroshio or the Agulhas retroreflection. Outside of these regions and small parts of the shelf, the estimation works very well. The pattern and amplitude of the estimated fluxes from GIGATL1 without simulated tides are very close to those estimated from JASON-3 data (Fig. 1). However, for the observations, higher fluxes are estimated in the Gulf Stream extension, the northern Brazil Malvinas Confluence, and the Agulhas ring path, which is consistent with higher mesoscale eddy activity in the observations (Fig. 3a and 3b). The largest differences between the area-averaged original and estimated geostrophic Π occur in April, where the maximum flux event is a bit overestimated (bottom panels Fig. 4c and 4d). Furthermore, the weak summer inverse cascade is slightly overestimated. This contributes to a slightly reduced amplitude of the seasonal cycle of the estimated flux compared to the original flux.

The horizontal scale of a SSH feature in the two-dimensional field may differ from that identified from the SSH along a track that cuts through the same feature. For example, if waves do not propagate in the direction of the track, they will appear to be associated with a larger wavelength along the track. Or if a track cuts through a circular eddy and does not cross its center, the eddy will appear to be smaller from the track information. The fact that the flux estimated from the one-dimensional SSH data agrees with that from the two-dimensional original shows that the estimation procedure corrects for this issue. We hypothesize that, on average, shorter scale features erroneously imprint at larger scales, and that the decreasing C with increasing scale corrects for this by reducing the pre-estimate (eq. (1) without C) more at larger scales. Future research needs to address the question, why the estimation works.

266 Data availability statement

267 The data to reproduce the figures of the present paper can be accessed at <https://doi.org/10.17882/96675>. Furthermore,
268 with the same link, the transition scale from balanced to unbalanced flows as well as the estimated scale kinetic energy
269 flux can be accessed. The ocean model output used for this study is too large for an online upload. The full JASON-3 data
270 used for this study is available at https://data.marine.copernicus.eu/product/SEALEVEL_GLO_PHY_L3_MY_008_062/services. The coastline shown in the Figures has been taken from www.naturalearthdata.com/downloads/110m-physical-vectors/.

273 Code availability statement

274 All the code to reproduce the study is available at <https://doi.org/10.17882/96675>. The scale kinetic energy flux
275 computations based on the two-dimensional model data has thereby been performed with a modified version of the code
276 published at <https://doi.org/10.5281/zenodo.4486265>.

277 References

- 278 1. Ferrari, R. & Wunsch, C. Ocean circulation kinetic energy: Reservoirs, sources, and sinks. *Annu. Rev. Fluid Mech.* **41**,
279 253–282 (2009).
- 280 2. Lévy, M. *et al.* Modifications of gyre circulation by sub-mesoscale physics. *Ocean. Model.* **34**, 1–15 (2010).
- 281 3. Hurlburt, H. E. & Hogan, P. J. Impact of 1/8° to 1/64° resolution on Gulf Stream model–data comparisons in basin-scale
282 subtropical Atlantic Ocean models. *Dyn. Atmospheres Ocean.* **32**, 283–329 (2000).
- 283 4. Chassignet, E. P. & Xu, X. Impact of horizontal resolution (1/12° to 1/50°) on gulf stream separation, penetration, and
284 variability. *J. Phys. Oceanogr.* **47**, 1999–2021 (2017).
- 285 5. Schubert, R., Gula, J. & Biastoch, A. Submesoscale flows impact Agulhas leakage in ocean simulations. *Commun. Earth
286 & Environ.* **2**, 1–8 (2021).
- 287 6. Scott, R. B. & Wang, F. Direct evidence of an oceanic inverse kinetic energy cascade from satellite altimetry. *J. Phys.
288 Oceanogr.* **35**, 1650–1666 (2005).
- 289 7. Molemaker, M. J., McWilliams, J. C. & Dewar, W. K. Submesoscale instability and generation of mesoscale anticyclones
290 near a separation of the California Undercurrent. *J. Phys. Oceanogr.* **45**, 613–629 (2015).
- 291 8. Schubert, R., Schwarzkopf, F. U., Baschek, B. & Biastoch, A. Submesoscale impacts on mesoscale Agulhas dynamics. *J.
292 Adv. Model. Earth Syst.* **11**, 2745–2767 (2019).
- 293 9. Jansen, M. & Ferrari, R. Macroturbulent equilibration in a thermally forced primitive equation system. *J. atmospheric
294 sciences* **69**, 695–713 (2012).
- 295 10. Tulloch, R., Marshall, J., Hill, C. & Smith, K. S. Scales, growth rates, and spectral fluxes of baroclinic instability in the
296 ocean. *J. Phys. Oceanogr.* **41**, 1057–1076 (2011).
- 297 11. Arbic, B. K., Polzin, K. L., Scott, R. B., Richman, J. G. & Shriver, J. F. On eddy viscosity, energy cascades, and the
298 horizontal resolution of gridded satellite altimeter products. *J. Phys. Oceanogr.* **43**, 283–300 (2013).
- 299 12. Qiu, B., Chen, S., Klein, P., Sasaki, H. & Sasai, Y. Seasonal mesoscale and submesoscale eddy variability along the North
300 Pacific Subtropical Countercurrent. *J. Phys. Oceanogr.* **44**, 3079–3098 (2014).
- 301 13. Wang, S., Liu, Z. & Pang, C. Geographical distribution and anisotropy of the inverse kinetic energy cascade, and its role in
302 the eddy equilibrium processes. *J. Geophys. Res. Ocean.* **120**, 4891–4906 (2015).
- 303 14. Rhines, P. B. Waves and turbulence on a beta-plane. *J. Fluid Mech.* **69**, 417–443 (1975).
- 304 15. Capet, X., McWilliams, J. C., Molemaker, M. J. & Shchepetkin, A. Mesoscale to submesoscale transition in the California
305 Current System. Part I: Flow structure, eddy flux, and observational tests. *J. Phys. Oceanogr.* **38**, 29–43 (2008).
- 306 16. Soh, H. S. & Kim, S. Y. Diagnostic characteristics of submesoscale coastal surface currents. *J. Geophys. Res. Ocean.* **123**,
307 1838–1859 (2018).
- 308 17. Schubert, R., Gula, J., Greatbatch, R. J., Baschek, B. & Biastoch, A. The submesoscale kinetic energy cascade: Mesoscale
309 absorption of submesoscale mixed layer eddies and frontal downscale fluxes. *J. Phys. Oceanogr.* **50**, 2573–2589 (2020).
- 310 18. Balwada, D., Xie, J.-H., Marino, R. & Feraco, F. Direct observational evidence of an oceanic dual kinetic energy cascade
311 and its seasonality. *Sci. Adv.* **8**, eabq2566 (2022).

- 312 19. Garabato, A. C. N. *et al.* Kinetic energy transfers between mesoscale and submesoscale motions in the open ocean's upper
313 layers. *J. Phys. Oceanogr.* **52**, 75–97 (2022).
- 314 20. Qiu, B., Nakano, T., Chen, S. & Klein, P. Bi-Directional Energy Cascades in the Pacific Ocean From Equator to Subarctic
315 Gyre. *Geophys. Res. Lett.* **49**, e2022GL097713 (2022).
- 316 21. Leonard, A. Energy cascade in large-eddy simulations of turbulent fluid flows. In *Advances in geophysics*, vol. 18, 237–248
317 (Elsevier, 1975).
- 318 22. Germano, M. Turbulence: the filtering approach. *J. Fluid Mech.* **238**, 325–336 (1992).
- 319 23. Eyink, G. L. Locality of turbulent cascades. *Phys. D: Nonlinear Phenom.* **207**, 91–116 (2005).
- 320 24. Aluie, H., Hecht, M. & Vallis, G. K. Mapping the energy cascade in the North Atlantic Ocean: the coarse-graining
321 approach. *J. Phys. Oceanogr.* **48**, 225–244 (2018).
- 322 25. Steinberg, J. M., Cole, S. T., Drushka, K. & Abernathey, R. P. Seasonality of the Mesoscale Inverse Cascade as Inferred
323 from Global Scale-Dependent Eddy Energy Observations. *J. Phys. Oceanogr.* (2022).
- 324 26. Contreras, M., Renault, L. & Marchesiello, P. Understanding Energy Pathways in the Gulf Stream. *J. Phys. Oceanogr.*
325 (2022).
- 326 27. Srinivasan, K., Barkan, R. & McWilliams, J. C. A forward energy flux at submesoscales driven by frontogenesis. *J. Phys.*
327 *Oceanogr.* **53**, 287–305 (2023).
- 328 28. Vergara, O., Morrow, R., Pujol, M.-I., Dibarboore, G. & Ubelmann, C. Global submesoscale diagnosis using along-track
329 satellite altimetry. *Ocean. Sci.* **19**, 363–379 (2023).
- 330 29. Lahaye, N., Gula, J. & Roullet, G. Sea surface signature of internal tides. *Geophys. Res. Lett.* **46**, 3880–3890 (2019).
- 331 30. Lawrence, A. & Callies, J. Seasonality and spatial dependence of meso-and submesoscale ocean currents from along-track
332 satellite altimetry. *J. Phys. Oceanogr.* (2022).
- 333 31. Qiu, B. *et al.* Seasonality in Transition Scale from Balanced to Unbalanced Motions in the World Ocean. *J. Phys. Oceanogr.*
334 **48**, 591–605 (2018).
- 335 32. Storer, B. A., Buzzicotti, M., Khatri, H., Griffies, S. M. & Aluie, H. Global energy spectrum of the general oceanic
336 circulation. *Nat. communications* **13**, 1–9 (2022).
- 337 33. Xu, Y. & Fu, L.-L. The effects of altimeter instrument noise on the estimation of the wavenumber spectrum of sea surface
338 height. *J. Phys. Oceanogr.* **42**, 2229–2233 (2012).
- 339 34. Dufau, C., Orsztynowicz, M., Dibarboore, G., Morrow, R. & Le Traon, P.-Y. Mesoscale resolution capability of altimetry:
340 Present and future. *J. Geophys. Res. Ocean.* **121**, 4910–4927 (2016).
- 341 35. Klein, P. *et al.* Ocean-scale interactions from space. *Earth Space Sci.* **6**, 795–817 (2019).
- 342 36. Gula, J., Theetten, S., Cambon, G. & Roullet, G. Description of the GIGATL simulations, DOI: [10.5281/zenodo.4948523](https://doi.org/10.5281/zenodo.4948523)
343 (2021).
- 344 37. Shchepetkin, A. & McWilliams, J. C. The Regional Oceanic Modeling System (ROMS): A split-explicit, free-surface,
345 topography-following- coordinate ocean model. *Ocean. Meteorol.* **9**, 347–404 (2005).
- 346 38. Arakawa, A. & Lamb, V. R. Computational design of the basic dynamical processes of the UCLA general circulation
347 model. *Gen. circulation models atmosphere* **17**, 173–265 (1977).
- 348 39. Carton, J. & Giese, B. A reanalysis of ocean climate using Simple Ocean Data Assimilation (SODA). *Mon. Weather. Rev.*
349 **136**, 2999–3017 (2008).
- 350 40. Renault, L., Masson, S., Arsouze, T., Madec, G. & McWilliams, J. C. Recipes for how to force oceanic model dynamics. *J.*
351 *Adv. Model. Earth Syst.* **12**, e2019MS001715 (2020).

352 Acknowledgements

353 The authors gratefully acknowledges support from the French National Agency for Research (ANR) through the project
354 DEEPER (ANR-19-CE01-0002-01). J.G. further gratefully acknowledges support from ISblue “Interdisciplinary graduate
355 school for the blue planet” (ANR-17- EURE-0015).

356 **Author contributions**

357 R.S. and J.G. designed the study. J.G. performed the numerical model simulations. O.V. computed the monthly climatology of
358 the transition scale from balanced to unbalanced flows. R.S. developed and executed all other analysis, produced the figures
359 and wrote the text. J.G. and O.V. contributed to the discussion of the results and the writing of the manuscript.

360 **Competing interests**

361 The authors declare no competing interests.

The open ocean kinetic energy cascade is strongest in late winter and spring

René Schubert^{1,*}, Oscar Vergara², and Jonathan Gula^{1,3}

¹University of Brest, CNRS, IRD, Ifremer, Laboratoire d’Océanographie Physique et Spatiale (LOPS), IUEM, Brest, France

²Collecte Localisation Satellites (CLS), Ramonville Saint-Agne, France

³Institut Universitaire de France (IUF), France

*corresponding author, rene.schubert@univ-brest.fr

Abstract

The oceanic kinetic energy cascade, the flux of kinetic energy between currents of different horizontal scales, shapes the structure of the global ocean circulation and the associated heat, salt, nutrient, and oxygen fluxes. Here, we show with a numerical ocean simulation that the surface geostrophic cascade can be estimated from satellite altimetry observations and present its regional distribution and seasonal cycle at scales of 40 to 150 km for large parts of the global ocean based on observations. The time-mean cascade is inverse (towards larger scales), strongest in large-scale current systems, and decreases with distance from these systems. In the open ocean, the inverse cascade is associated with a maximum in late winter at the smallest scales studied, which transitions to scales larger than 100 km within two to three months, consistent with the widespread absorption of mixed-layer eddies in spring.

1 Introduction

Ocean motions can be decomposed into movements at different horizontal scales ranging from large-scales ($\mathcal{O}(1000 \text{ km})$) through mesoscales ($\mathcal{O}(100 \text{ km})$) and submesoscales ($\mathcal{O}(100 \text{ m}) - \mathcal{O}(10 \text{ km})$) to microscales ($<\mathcal{O}(100 \text{ m})$). The flux of kinetic energy (KE) between ocean currents at different scales, the KE cascade, plays a key role in several aspects of global climate. First, in combination with the transformation of KE into available potential energy (and vice versa), the cascade mediates the balance between the oceans forcing by the atmosphere, primarily by wind at large scales, and the dissipation of KE into heat at molecular scales¹. Second, the KE cascade controls the scale-distribution of KE including the strength of the subtropical gyre², the strength and position of large-scale currents such as the Gulf Stream^{3,4}, the strength of inter-ocean exchanges such as Agulhas leakage⁵, and the strength and distribution of ocean mesoscale eddies^{6–8} and thus the associated transports of heat, salt, nutrients, and oxygen. Third, through ocean-atmosphere interactions, the ocean and atmosphere KE cascades determine their response times to external forcing⁹. This induces a modulation of the atmospheric circulation by the oceanic KE cascade. In addition to being a key component of the climate system, understanding the KE cascade is critical for the validation and development of climate models, particularly regarding the parameterization of the sub-grid-scale energetic fluxes and dissipation.

For the large mesoscales, the KE flux was computed from gridded sea-surface height data that were interpolated from along-track satellite altimetry measurements on a regular 0.25° and daily grid (AVISO) assuming geostrophy and an f-plane^{6,10–12}. The results showed an inverse cascade (from smaller to larger scales) at scales larger than about 75 km and a forward cascade (from larger to smaller scales) at smaller scales. While the forward cascade was later found to be an artifact of the filtering and interpolation technique onto the regular grid, the inverse cascade at larger scales was found to be robust to filtering^{11,12}. At scales of the maximum inverse flux (about 200 km), the cascade has been shown to be orders of magnitude smaller in the open ocean compared to regions of strong current systems¹³. This is not surprising, as the inverse cascade is stopped at smaller scales in the open ocean, for example due to the Rhines effect¹⁴. Substantial inverse fluxes occur at these scales only in the large-scale current systems, where very large mesoscale eddies form as a consequence of large-scale instabilities and interact with the large-scale currents. Regional submesoscale-permitting simulations and regional observations have shown that the inverse cascade extends into the submesoscales to scales of the mixed-layer Rossby radius of deformation (about 15 km)^{12,15–20}. Applying a filtering approach for computing the KE flux^{21–24} to submesoscale-permitting model data, it was found that the underlying process of the submesoscale inverse cascade is primarily the absorption of submesoscale mixed layer eddies by mesoscales eddies¹⁷. Consistently, the maximum of the submesoscale inverse flux has been found to occur immediately after the submesoscale season in late winter and to shift to larger scales in spring¹⁷. Based on observations, the existence of the submesoscale inverse KE cascade and its seasonality could only be demonstrated for small ocean regions^{16,18–20}. Indirect evidence that this submesoscale inverse cascade is active in large parts of the global ocean has recently been provided by

50 high-resolution satellite products²⁵. Recent model studies have applied Helmholtz decomposition and principal strain coordinate
 51 transformation prior to the computation of the scale KE flux, and have shown that the inverse cascade is primarily driven by
 52 geostrophically balanced flows^{26,27}. This confirms that it should be possible to analyze the near-surface inverse KE cascade on
 53 the basis of sea-surface height.

54
 55 In this study, we provide an observation-based estimate of the surface geostrophic KE cascade and its seasonal cycle at
 56 scales of 40-150 km in large parts of the global ocean. We use information on the dynamics in the respective scale-band from
 57 satellite along-track altimetry data measured by JASON-3 as well as from a submesoscale-permitting simulation of the Atlantic.
 58 The KE flux can not be computed directly from along-track sea-surface height. However, using the simulation, we prove that it
 59 is possible to estimate the KE flux from the simulated sea-surface height along the tracks of JASON-3 and apply the proposed
 60 estimation technique to the actual measurements.

61 2 Results

If the measured along-track absolute dynamic topography (η) is dominated by geostrophic flows, the across-track f-plane geostrophic flow component can be computed as $u = -\frac{g}{f}\eta_y$, where $g = 9.81 \text{ m s}^{-2}$ is the gravitational acceleration, $f = 2\Omega \sin(2\pi \frac{\theta}{360^\circ})$ is the Coriolis parameter with the Earth's angular speed $\Omega = \frac{2\pi}{86400} \text{ s}^{-1}$ and the latitude θ , and y is the along-track direction with increasing latitude. Partial derivatives of a with respect to b are written here and in the following as $\frac{\partial a}{\partial b} = a_b$. For this study, we use five years of tide-corrected and filtered measurements of η taken by the JASON-3 satellite along the tracks shown in Figure 1a. From these, we estimate the surface geostrophic $5^\circ \times 5^\circ$ domain-averaged scale-KE flux through a specific scale L as

$$\langle \Pi_{est} \rangle = -C(L)\rho_0 \overline{\langle u^2 \rangle - \overline{uu} \rangle} \langle |\bar{u}_y| \rangle, \quad (1)$$

62 where angle brackets indicate averages over $5^\circ \times 5^\circ$ subdomains for each measurement cycle, C is an estimation coefficient
 63 identified from a numerical ocean simulation, and $\rho_0 = 1024 \text{ kg m}^{-3}$ is the standard density. The overlines denote fields
 64 convoluted with a tophead kernel whose length is equal to that of the respective scale L and which is normalized so that it
 65 integrates to 1. The computation of C and the proof that the proposed estimation works is given in section 3.

66 If η is not dominated by geostrophic flows, the computation of geostrophic currents from the measurements fails. A lower
 67 bound for the scales at which the respective gradients of η can be used to derive geostrophic flows is provided by the transition
 68 scale from balanced to unbalanced flows T . T is estimated from the JASON-3 along-track data with a previously published
 69 method²⁸ and is averaged over the same $5^\circ \times 5^\circ$ grid on which we estimate the scale KE flux. T is associated with lower
 70 values in regions with strong balanced flows (large-scale currents and surface eddy pathways) and higher values in regions with
 71 weak balanced flows (weak eddy activity)²⁸. Furthermore, T is associated with a seasonal cycle, with lower values in spring
 72 when there are more balanced submesoscale vortices, and higher values in summer and autumn when the surface signature
 73 of internal waves is amplified²⁹. In Figures 1 and 2 we highlight with black lines the regions, scales and seasons where the
 74 results are partially corrupted by too strong imprints of unbalanced flows into the absolute dynamic topography measurements.
 75 Furthermore, we exclude the tropics between $15^\circ S$ and $15^\circ N$ from our analysis, because the baroclinic mode-1 and mode-2
 76 diurnal tides significantly affect the SSH-spectrum³⁰ there, and consequently T exceeds 75 km throughout the year³¹.

77 2.1 The time-mean scale KE flux

The time-mean estimated fluxes at scales of 60, 140 and 200 km are shown in Figure 1. The largest (inverse) fluxes occur at all
 79 scales in regions of very strong near-surface current systems, such as the Gulf-Stream - North-Atlantic-Current system, the
 80 Agulhas system, the Brazil-Malvinas-Confluence or the Kuroshio. The further away from the large-scale currents, the smaller
 81 the fluxes. Fluxes at 140 km and 200 km scales are very close to each other and have substantial amplitudes almost only in
 82 regions of large-scale current systems. At 200 km, the pattern is very similar to the one presented in a previous study based on
 83 gridded AVISO data¹³. At this scale, almost no time-mean fluxes are found in the open ocean. At 60 km, fluxes of about 10-20
 84 mW km⁻¹ m⁻³ occur in large parts of the mid-latitudes. This is consistent with wide-spread mixed-layer instabilities leading
 85 to the formation of submesoscale eddies, which are subsequently absorbed by the mesoscales¹⁷.

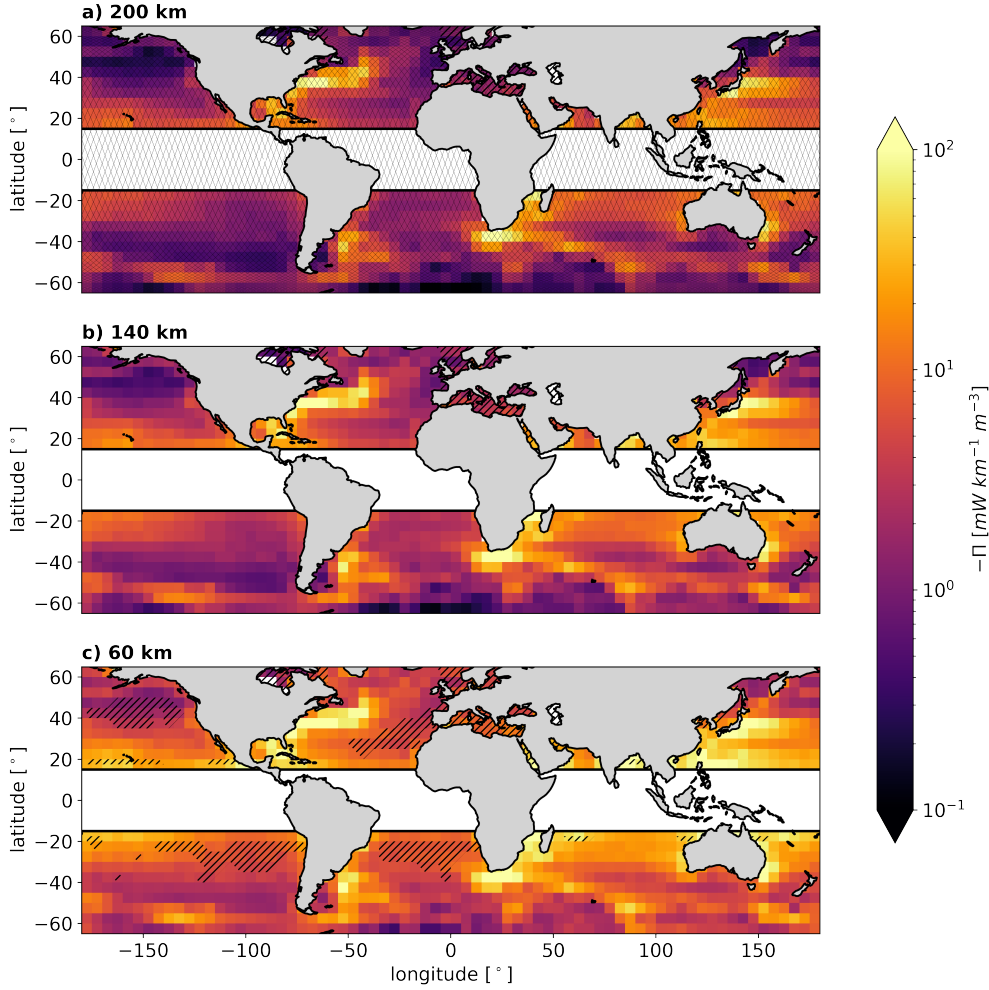


Figure 1. The time-mean inverse scale kinetic energy flux The time-mean inverse scale kinetic energy flux $-\Pi_{est}$ from JASON-3 SSH at scales of 200 km (a), 140 km (b), and 60 km (c). In a), thin black lines show the JASON-3 tracks. Hatches mark regions where the time-mean transition scale from balanced to unbalanced flows T is larger than the scale, $-\Pi_{est}$ is shown for, and thus, where the results have to be interpreted with care.

87 2.2 The seasonal cycle of the scale KE flux

88 The seasonal cycle of Π_{est} and its scale-distribution are shown in Figure 2. At 60 km, the anomalies of the FMA-mean (Fig.
 89 2a) and the ASO-mean (Fig. 2b) relative to the 2017-2021 mean flux show enhanced inverse fluxes in spring and reduced
 90 inverse fluxes in autumn for most open ocean regions. This is consistent with a previously published map of the seasonal
 91 difference in geostrophic KE computed from along-track altimetry²⁵. In the open ocean, enhanced fluxes occur in winter and
 92 spring with a maximum in early spring (February in the Northern Hemisphere and July in the Southern Hemisphere) at 40 km
 93 scale (Fig. 2c and 2d). During the following three to four months, enhanced fluxes occur at increasingly larger scales. Deeper
 94 mixed layer depths in winter allow for the accumulation of more available potential energy at mixed-layer fronts. Mixed-layer
 95 baroclinic instability of the fronts releases this potential energy into KE in the form of mixed-layer eddies²⁵. These eddies have
 96 a diameter on the order of the mixed-layer Rossby deformation radius (about 15 km) and are stronger and more frequent in
 97 winter. Subsequently, these eddies grow and are absorbed by mesoscale eddies. The absorption process takes about 2-3 months,
 98 resulting in a shift of the maximum scale KE flux from late winter at 30 km to late spring at 140 km. This climatological
 99 scale-time pattern of the observation-based estimated inverse flux is consistent with that of the power-spectral density of KE
 100 computed from AVISO³² and along-track altimetry²⁵. The same consistency was also found in a simulation of the open ocean
 101 near the Agulhas-system¹⁷. In regions of strong large-scale flows, in particular the Gulf Stream and Kuroshio extensions, the
 102 Brazil Malvinas Confluence, and the Agulhas region and Return Current, the estimated fluxes at 60 km mainly show an opposite
 103 seasonal cycle to that of the open ocean. This is consistent with results from a recent model study of the Gulf Stream, which

104 found a stronger seasonal cycle of the balanced cascade outside of the Gulf Stream core, including a scale-shift of the maximum
 105 inverse flux and a reduced seasonality without a scale-shift of the maximum in a region that partially includes the Gulf Stream²⁶.
 106 Furthermore this is consistent with previously published results on along-track altimetry based geostrophic KE levels, which
 107 revealed an opposite seasonal cycle within the strong current-systems²⁵. We speculate that the reason for this phenomenon is
 108 that other energetic submesoscale and mesoscale processes overcome the seasonal cycle of mixed-layer instabilities and the
 109 subsequent inverse cascade of the resulting mixed layer eddies. In the future, these other processes need to be identified.

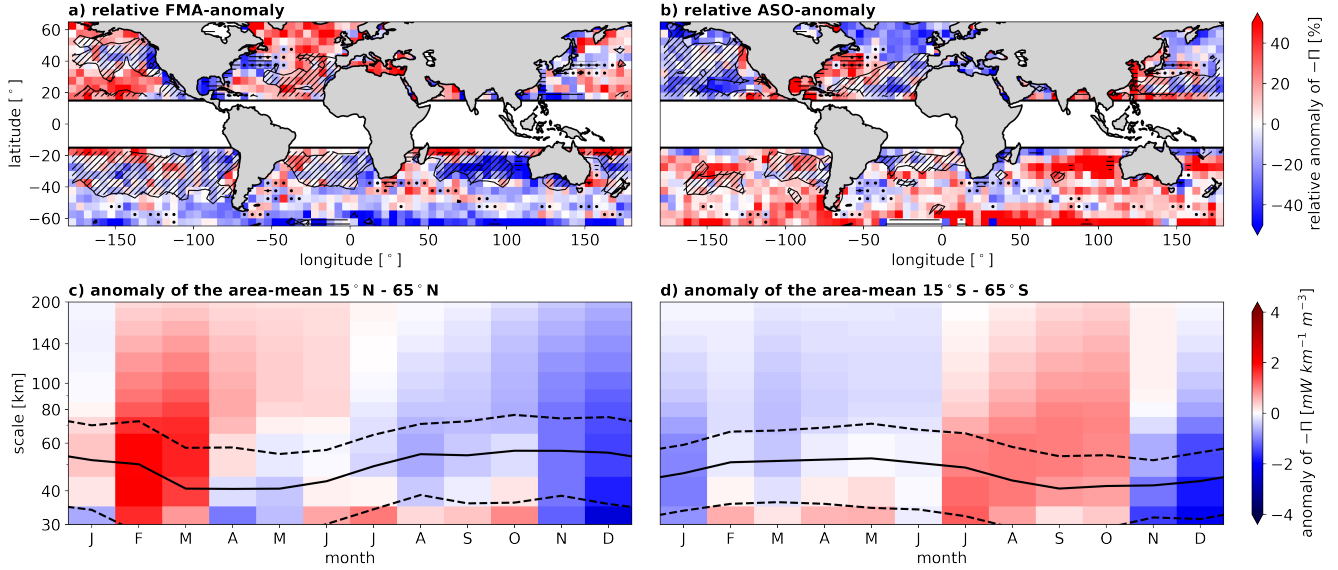


Figure 2. The seasonal cycle of the inverse scale kinetic energy flux Monthly climatological anomalies of the scale kinetic energy flux $-\Pi_{est}$ from JASON-3 with respect to the 2017-2021 mean. Red (blue) colors mark enhanced (reduced) inverse cascade. Shown are the relative anomalies for the FMA-mean (**a**) and ASO-mean (**b**) flux at 60 km, as well as the anomalies for the area-mean flux between 15°N and 65°N (**c**), and between 15°S and 65°S (**d**). Contour lines and diagonal hatches mark where the maximum transition scale from balanced to unbalanced flows T is in the respective season larger than 60 km and thus, where the results are potentially erroneous due to non-geostrophic gradients of η . Regions of strong large-scale currents are excluded before the area-averaging for the bottom panels. They are identified by the temporal standard deviations of 2017-2021 AVISO-SSH averaged over $5^{\circ} \times 5^{\circ}$ domains larger than 20 cm (dotted) and by anomalies of the KE flux that are larger than $15 \text{ mW km}^{-1} \text{ m}^{-3}$ at 60 km (horizontal hatches). The respective area-mean T (solid line) plus and minus one standard deviation (dashed lines) are shown in **c** and **d**.

110 Particularly in summer, in regions of weak mesoscale activity at scales of 70 km and smaller, the measured absolute dynamic
 111 topography is not dominated by balanced flows and $-\Pi_{est}$ gives spuriously enhanced values. This manifests itself in a spurious
 112 reduction or reversal of the seasonal cycle at 60 km in regions such as the North East Pacific or the Central Atlantic, where the
 113 maximum T of the respective season is larger than 60 km (contours and hatches in Fig. 2a and 2b), as well as small secondary
 114 maxima of $-\Pi_{est}$ in summer (August in the Northern Hemisphere and February in the Southern Hemisphere) mainly at scales
 115 smaller than 70 km (Fig. 2c and 2d).

116 3 Methods

117 3.1 JASON-3 satellite along-track altimetry data

118 JASON-3 measures the absolute dynamic topography η , the sum of the sea-level anomaly and the mean dynamic topography,
 119 between 66°S and 66°N with an along-track resolution of about 6 km at 1 Hz and a repeated measurement of each track every
 120 10th day. Below scales of 25-35 km, JASON-class data are associated with noise^{33,34}. This noise is associated with a seasonal
 121 cycle that is similar, but not identical, to that of the submesoscale KE level³⁴ (at least north of 40°S ³⁵): higher noise and
 122 submesoscale KE in winter and lower in summer. The sea-level anomaly is available in an original (unfiltered) and a low-pass
 123 "filtered" version. Fourier-analysis shows that the seasonal cycle of power spectral density of the unfiltered η has deviations
 124 from 20 km on all scales larger than 30 km (Fig. 3e), indicating that the seasonal cycle at these scales is not corrupted by
 125 measurement noise. Furthermore, for this study, we use the tide-corrected data, where the barotropic tides and the coherent part
 126 of the baroclinic tides for modes M2, K1, O1 and S2 have been removed from the data. Note, however, that there is a residual

127 effect of tides that cannot be corrected. Note also that η is the sea-surface height (SSH) corrected by the geoid. Since the geoid
128 is associated with very large scales, this correction is not relevant for the analysis presented in this study. Therefore, η is also
129 referred to as SSH in the following.

130 **3.2 GIGATL1 simulation**

131 The GIGATL1 simulation³⁶ used here has been performed with the Coastal and Regional Ocean CCommunity model (CROCO,
132 10.5281/zenodo.7415055), which is based on the Regional Ocean Modeling System (ROMS³⁷). The integration is performed
133 on an Arakawa C-grid³⁸ using 100 vertical terrain-following sigma-levels where the bathymetry is taken from the SRTM30plus
134 dataset. Vertical mixing is parameterized with the k-epsilon turbulence closure scheme with applied Canuto A stability function.
135 No explicit lateral diffusivities and viscosities are used. The effect of bottom friction is parameterized with a logarithmic law
136 using a roughness length of 0.01 m. The GIGATL1 grid is orthogonal based on an oblique Mercator projection and designed
137 to have nearly uniform spacing in both horizontal dimensions. The grid spacing varies from 1 km at the central longitude
138 of the grid to 735 m at the west and east extremes of the grid. A simulation with a grid-spacing three times as large as the
139 one of GIGATL1, "GIGATL3", has been initialized in January 2004. Initialization fields and boundary conditions are from
140 Simple Ocean Data Assimilation (SODA³⁹). GIGATL1 is initialized from the restarts of GIGATL3 in July 2007 and integrated
141 twice, one experiment with simulated tides and one experiment without simulated tides. All simulations are forced by hourly
142 atmospheric forcing data from the Climate Forecast System Reanalysis (CFSR) with a bulk formulation and a stress correction
143 approach to parameterize the surface ocean current feedback to the atmosphere⁴⁰. Barotropic tidal forcing at the boundaries
144 and tidal potential and self attraction from TPXO7.2 and GOT99.2b are applied to GIGATL3 and GIGATL1 with tides. In this
145 study, we analyze snapshots every fifth day over the period April 2008 to March 2009 for both simulations.

146 **3.3 Model Validation**

147 The temporal standard deviation of SSH, computed from daily averages during Apr 2008 - Mar 2009 averaged onto the AVISO
148 grid, shows similar large-scale patterns for GIGATL1 without simulated tides and AVISO (Fig. 3a and 3b). The largest values
149 occur in the region of the Gulf Stream, North Atlantic Current and Brazil Malvinas Confluence systems, moderate values in
150 the surrounding ocean, as well as in the Agulhas ring path, the Azores Current, and the North Equatorial Counter Current,
151 and low values above the shelves and in the central subtropical gyres. The simulated SSH variabilities are smaller than in the
152 observations in the Gulf Stream extension, the Brazil Current extension, and the Agulhas Ring Path, and larger north of 50°N.
153 The standard deviation of SSH in the Northwest-Corner and the North Atlantic Current are in remarkably good agreement.
154 The too low simulated SSH variability in the Agulhas ring path is a result of the monthly boundary conditions applied at the
155 southern boundary of the domain, which are not frequent enough to resolve the full variability of the energetic eddies drifting
156 out of the Agulhas region into the Atlantic.

157 Time-mean horizontal wavenumber spectra computed from SSH at JASON-3 tracks in a $20^\circ \times 20^\circ$ domain in the open
158 ocean show similar results for JASON-3 and GIGATL1 without simulated tides (Fig. 3c). For comparison, the GIGATL1 SSH
159 is extracted at the measurement locations of JASON-3 from model snapshots every fifth day. The SSH-spectra from GIGATL1
160 without tides and the unfiltered, tide-corrected JASON-3 data show a very good agreement at scales larger than 60 km. At scales
161 smaller than 60 km, the spectrum of the observations shows higher values compared to the simulation, which could be due to
162 observational noise or unresolved processes. The spectrum of the filtered JASON-3 SSH follows that of the unfiltered down to
163 45 km, but with a shallower slope between 60 km and 45 km than in the simulation, which shows a k^{-4} slope down to 30 km.

164 Hovmöller plots of the monthly climatology of the SSH-spectrum for both the simulation and the observations (Fig. 3d
165 and 3e) show maxima that shift from winter at scales of $\mathcal{O}(10 \text{ km})$ to summer at scales of $\mathcal{O}(100 \text{ km})$ similar to the maximum
166 inverse cascade estimated from JASON-3 (Fig. 2c). This shift is consistent with previous results from AVISO and simulations^{17,32}, as well as with a maximum of submesoscale activity in winter and spring and a subsequent inverse cascade involving
167 the growth of submesoscale eddies and their absorption by mesoscale eddies¹⁷. For the simulation, the Hovmöller plot is more
168 patchy and shows the shift to larger scales one to two months later than in the observations. This can be due to the specific
169 conditions in the single simulated year, which is compared here to a five-year average from the observations.

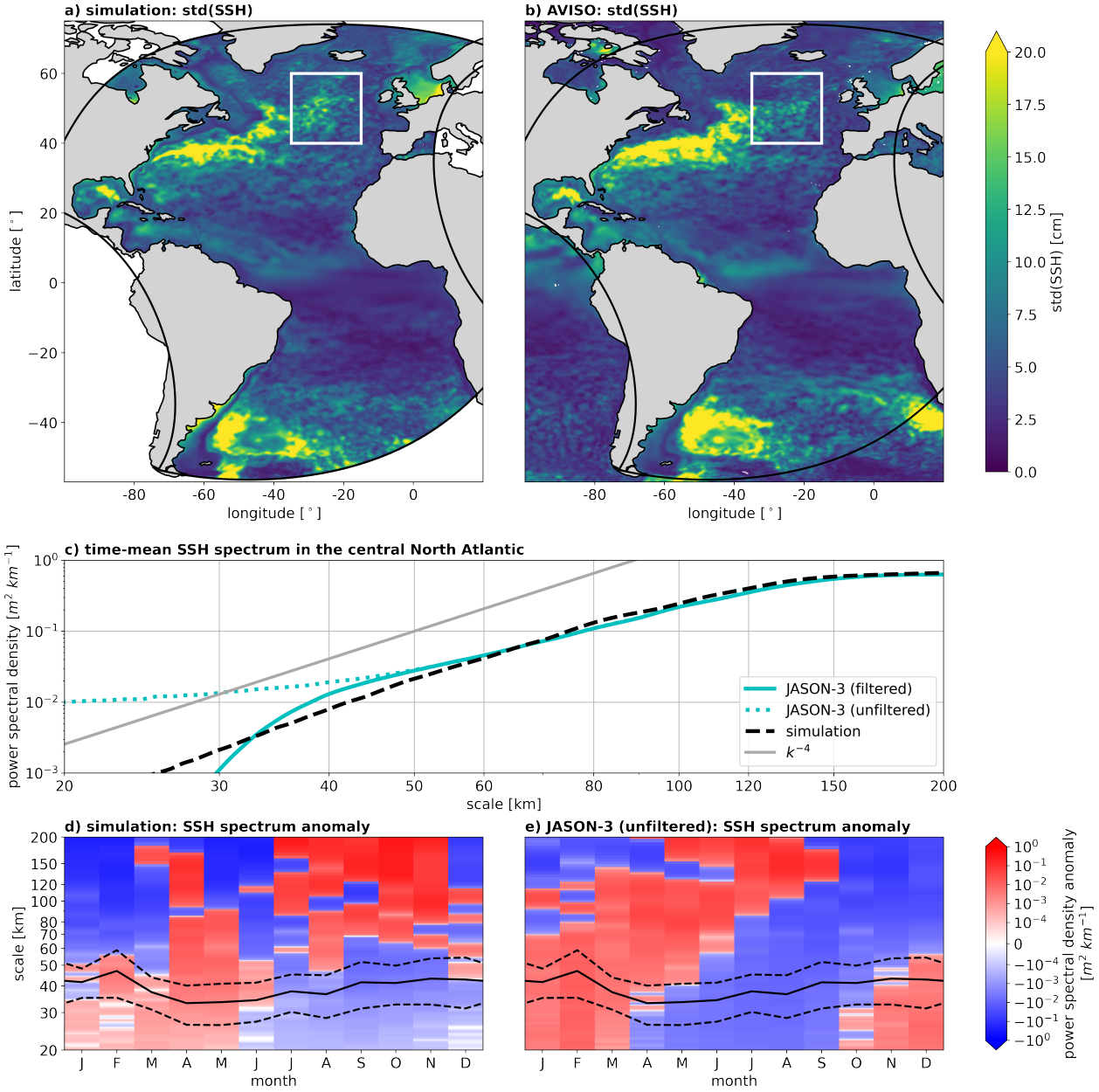


Figure 3. Model Validation The standard deviation of SSH computed from Apr 2008 - Mar 2009 daily mean fields of GIGATL1 without simulated tides (**a**) and AVISO (**b**). Thick black lines show the GIGATL1 domain, and the white box the region for which the Fourier-transform is performed for the middle and bottom panels. **c**) shows the time-mean SSH spectra and a gray straight line for the k^{-4} slope. **d**) and **e**) show Hovmöller plots of the monthly climatological anomalies of the SSH spectra with respect to the mean over the period Apr 2008 - Mar 2009 for **d**) and 2017-2021 for **e**). The respective area-mean T (solid line) plus and minus one standard deviation (dashed lines) are shown in **d**) and **e**).

173 3.4 The scale KE flux

With the filtering approach, the scale KE flux can be computed as

$$\Pi = -\rho_0[(\bar{u}^2 - \bar{u}^2)\bar{u}_x + (\bar{u}\bar{v} - \bar{u}\bar{v})(\bar{u}_y + \bar{v}_x) + (\bar{v}^2 - \bar{v}^2)\bar{v}_y], \quad (2)$$

174 where u and v are the total horizontal velocity components in perpendicular directions x and y ²¹⁻²⁴. The overlines denote fields
 175 convolved with a two-dimensional top-head kernel whose diameter is equal to that of the respective scale L and which is
 176 normalized by the respective enclosed area so that it integrates to 1. Π is only computed if the full kernel area is filled with data.

177 To reduce the memory requirement for convolutions in the computation of Π , which increases exponentially with the respective
 178 scale, u and v are first averaged within 5×5 grid-cell boxes. This has almost no effect on the results, as the variations of the
 179 simulated values on the near-grid-scale are very small. Due to limits in computational time and storage, the computations were
 180 only feasible for snapshots every fifth day. While this does not affect the results for area-averages, the results for time-averages
 181 may contain aliasing effects.
 182

183 Large amplitudes of surface time-mean Π occur mainly in regions of strong current systems. While the Gulf Stream -
 184 North Atlantic Current and Brazil Malvinas Confluence systems show time-mean fluxes of both signs at 60 km scales, the
 185 equatorial current system is associated with a time-mean forward cascade (Fig. 4a). The area-mean flux for a large region in the
 186 North Atlantic, shows a dominant forward cascade in summer and autumn (JJASON) and a dominant inverse cascade in winter
 187 and spring (DJFMAM) (lower panel in Fig. 4a). The maximum inverse cascade shifts by a few months with increasing scale.
 188 This is consistent with the absorption of the winter-time submesoscale vortices by the mesoscales which takes this time¹⁷, and
 189 with the seasonal cycle of the SSH spectrum in the North Atlantic Current (Fig. 3d).
 190
 191

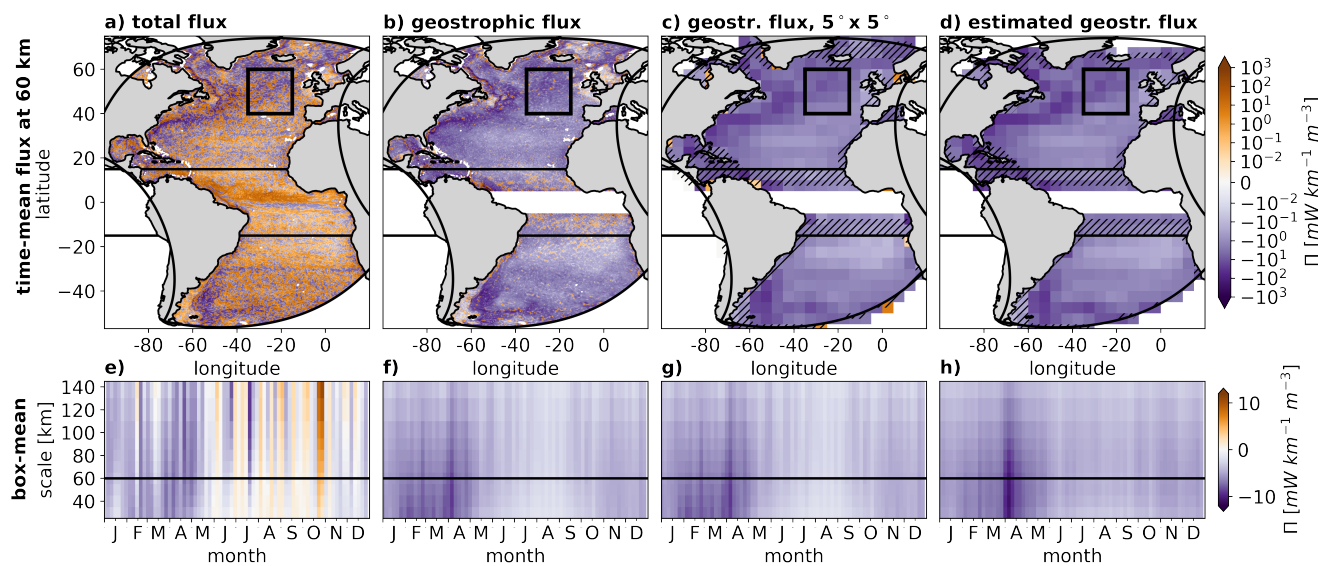


Figure 4. The simulated scale kinetic energy flux The scale kinetic energy flux Π computed from GIGATL1 without simulated tides in the period Apr 2008 - Mar 2009 from the total velocity (a), the geostrophic velocity (b), the geostrophic velocity and subsequently averaged over $5^\circ \times 5^\circ$ domains (c), and estimated with equation (1) from SSH cut from the simulation along JASON-3 tracks (d). The time-mean flux at 60 km scales is shown in (a) to (d). $15^\circ S$ and $15^\circ N$ are shown with black horizontal lines. Hatches mark regions that have been excluded for the computation of the estimation coefficient C . In (e) to (h), Hovmöller plots of the respective area-averaged flux in the North Atlantic are shown (domain marked with a black box in (a) to (d)). The scale of 60 km is marked with a black line.

192 The geostrophic scale KE flux can be computed by using (2), with the geostrophic velocity. Noisy large-amplitude time-mean
 193 geostrophic fluxes occur on the shelf, as well as in the tropics (Fig. 4b). Away from these regions, the time-mean geostrophic
 194 flux is inverse almost everywhere. When averaged over $5^\circ \times 5^\circ$ regions, the instantaneous geostrophic flux is only very rarely
 195 forward. In the time-mean, only a few regions near the coast or near the boundary of the domain show time-mean forward fluxes
 196 (Fig. 4c). Geostrophic fluxes averaged over the North Atlantic box show a dominant inverse cascade at all times and scales
 197 as well (bottom panels in Fig. 4b and 4c). The inverse cascade is maximum at the smallest investigated scales in February,
 198 March, and April, which shifts to April and May at scales of 100 km and larger. The similar timing and amplitude of the inverse
 199 cascade from the total velocity (Fig. 4a) support that balanced flows are primarily responsible for the inverse cascade, as shown
 200 in previous studies^{26,27}. Furthermore, this confirms that the near-surface winter and spring inverse cascade can be studied using
 201 SSH. However, for the interpretation of the geostrophic flux, one needs to be aware that the ageostrophic (net forward) cascade
 202 reduces the geostrophic (net inverse) cascade mainly at scales smaller than 40 km throughout the year (Fig. 4a). Note that the
 203 results presented here for the surface cascade from total velocities correspond to an extreme case, as forward fluxes are surface
 204 intensified and restricted to the very upper ocean, while the inverse cascade driven by the balanced flows extends deep into the

ocean^{17,27}. The estimate of the geostrophic flux presented in section 2 is therefore more representative of the cascade over the depth-range of surface intensified balanced flows than of the cascade directly at the surface.

3.5 Estimating the scale KE flux from along-track data

In order to access the smallest scales observed by satellite altimetry, we must use the non-gridded along-track SSH product. However, it is not possible to compute the geostrophic Π directly from along-track SSH, as one can only compute the across-track geostrophic velocity component. This implies that, of all the terms in (2), only the Leonard stress $\bar{u}^2 - \bar{u}^2$, and the along-track derivative \bar{u}_y are computable. For this study, we propose to estimate the flux with equation (1), which includes the product of these two terms giving the correct unit of a scale KE flux. Since $\bar{u}^2 - \bar{u}^2$ is always positive, using the absolute value of \bar{u}_y along with the minus sign means that the estimated geostrophic flux is globally inverse, consistent with what we found for the time- and area-averaged geostrophic fluxes in the simulations (Fig. 4c), with AVISO based observational studies at larger scales^{6,11}, and with theoretical studies that showed that the balanced flows are associated with inverse fluxes^{26,27}. However, in some shelf regions, $5^\circ \times 5^\circ$ averaged forward geostrophic fluxes do occur in our simulations, which implies that the estimated fluxes from JASON-3 need to be interpreted with care on the shelf. Trying to estimate the sign of the geostrophic flux directly, for example by using \bar{u}_y without taking its absolute value and removing the minus sign in equation (1), has not been successful.

We average both subterms in equation (1) over $5^\circ \times 5^\circ$ boxes, as the estimation works better the larger this region is, and as they are large enough to cover reasonable amounts of along-track data (which have a track-to-track distance of several degrees for ascending and descending tracks (Fig. 1a). This technique is associated with the inclusion of information from both horizontal directions, as the angle between ascending and descending tracks is large (Fig. 1a), and thus reduces the effect of the isotropy assumption that is necessarily made when one-dimensional data is cut from a two-dimensional field and then used to make a statement about that field.

The estimation coefficient C is identified from the simulations for each chosen scale by area- and time-averaging the term $\langle \Pi \rangle / (-\rho_0 \langle \tau_{uu} \rangle \langle |\bar{u}_y| \rangle)$, where $\langle \Pi \rangle$ is computed from the 5x5 grid-cell averaged SSH field and the divisor terms from the SSH extracted from the simulation along the JASON-3 tracks. For the final area-averaging of the term, regions near the coast and boundary of the simulation, where the respective $5^\circ \times 5^\circ$ domain includes only a small ocean area are excluded (shown hatched in Fig. 4c), as well as regions and times where $L < T$. For scales of [30,40,50,60,70,80,90,100,120,140,160,180,200] km, C is computed to be [0.32,0.26,0.23,0.22,0.20,0.19,0.18,0.17,0.15,0.14,0.13,0.12,0.11] and thus shows an exponential decay with larger scales. Computing C from a parallel simulation with simulated tides, gives similar values (see Supplementary Note 1 and Supplementary Figure 1).

Comparisons of the original and estimated time-mean fluxes at a scale of 60 km and their area-mean in the North Atlantic box show that the estimation reproduces the horizontal and temporal patterns and their amplitudes reasonably well (Fig. 4c and 4d). Large differences only show up in the Gulf Stream extension, where the flux is overestimated, and in a few shelf regions where the original flux is forward and thus cannot be estimated correctly with equation (1). The former may be due to the extreme non-isotropy of the core Gulf Stream extension and indicates that the fluxes are overestimated in similar energetic non-isotropic flows, such as the western Kuroshio or the Agulhas retroflection. Outside of these regions and small parts of the shelf, the estimation works very well. The pattern and amplitude of the estimated fluxes from GIGATL1 without simulated tides are very close to those estimated from JASON-3 data (Fig. 1). However, for the observations, higher fluxes are estimated in the Gulf Stream extension, the northern Brazil Malvinas Confluence, and the Agulhas ring path, which is consistent with higher mesoscale eddy activity in the observations (Fig. 3a and 3b). The largest differences between the area-averaged original and estimated geostrophic Π occur in April, where the maximum flux event is a bit overestimated (bottom panels Fig. 4c and 4d). Furthermore, the weak summer inverse cascade is slightly overestimated. This contributes to a slightly reduced amplitude of the seasonal cycle of the estimated flux compared to the original flux.

The horizontal scale of a SSH feature in the two-dimensional field may differ from that identified from the SSH along a track that cuts through the same feature. For example, if waves do not propagate in the direction of the track, they will appear to be associated with a larger wavelength along the track. Or if a track cuts through a circular eddy and does not cross its center, the eddy will appear to be smaller from the track information. The fact that the flux estimated from the one-dimensional SSH data agrees with that from the two-dimensional original shows that the estimation procedure corrects for this issue. We hypothesize that, on average, shorter scale features erroneously imprint at larger scales, and that the decreasing C with increasing scale corrects for this by reducing the pre-estimate (eq. (1) without C) more at larger scales. Future research needs to address the question, why the estimation works.

258 Data availability statement

259 The data to reproduce the figures of the present paper can be accessed at <https://doi.org/10.17882/96675>. Furthermore,
260 with the same link, the transition scale from balanced to unbalanced flows as well as the estimated scale kinetic energy
261 flux can be accessed. The ocean model output used for this study is too large for an online upload. The full JASON-3 data
262 used for this study is available at https://data.marine.copernicus.eu/product/SEALEVEL_GLO_PHY_L3_MY_008_062/services. The coastline shown in the Figures has been taken from www.naturalearthdata.com/downloads/110m-physical-vectors/.

265 Code availability statement

266 All the code to reproduce the study is available at <https://doi.org/10.17882/96675>. The scale kinetic energy flux
267 computations based on the two-dimensional model data has thereby been performed with a modified version of the code
268 published at <https://doi.org/10.5281/zenodo.4486265>.

269 References

- 270 1. Ferrari, R. & Wunsch, C. Ocean circulation kinetic energy: Reservoirs, sources, and sinks. *Annu. Rev. Fluid Mech.* **41**,
271 253–282 (2009).
- 272 2. Lévy, M. *et al.* Modifications of gyre circulation by sub-mesoscale physics. *Ocean. Model.* **34**, 1–15 (2010).
- 273 3. Hurlburt, H. E. & Hogan, P. J. Impact of 1/8° to 1/64° resolution on Gulf Stream model–data comparisons in basin-scale
274 subtropical Atlantic Ocean models. *Dyn. Atmospheres Ocean.* **32**, 283–329 (2000).
- 275 4. Chassignet, E. P. & Xu, X. Impact of horizontal resolution (1/12° to 1/50°) on gulf stream separation, penetration, and
276 variability. *J. Phys. Oceanogr.* **47**, 1999–2021 (2017).
- 277 5. Schubert, R., Gula, J. & Biastoch, A. Submesoscale flows impact Agulhas leakage in ocean simulations. *Commun. Earth
278 & Environ.* **2**, 1–8 (2021).
- 279 6. Scott, R. B. & Wang, F. Direct evidence of an oceanic inverse kinetic energy cascade from satellite altimetry. *J. Phys.
280 Oceanogr.* **35**, 1650–1666 (2005).
- 281 7. Molemaker, M. J., McWilliams, J. C. & Dewar, W. K. Submesoscale instability and generation of mesoscale anticyclones
282 near a separation of the California Undercurrent. *J. Phys. Oceanogr.* **45**, 613–629 (2015).
- 283 8. Schubert, R., Schwarzkopf, F. U., Baschek, B. & Biastoch, A. Submesoscale impacts on mesoscale Agulhas dynamics. *J.
284 Adv. Model. Earth Syst.* **11**, 2745–2767 (2019).
- 285 9. Jansen, M. & Ferrari, R. Macroturbulent equilibration in a thermally forced primitive equation system. *J. atmospheric
286 sciences* **69**, 695–713 (2012).
- 287 10. Tulloch, R., Marshall, J., Hill, C. & Smith, K. S. Scales, growth rates, and spectral fluxes of baroclinic instability in the
288 ocean. *J. Phys. Oceanogr.* **41**, 1057–1076 (2011).
- 289 11. Arbic, B. K., Polzin, K. L., Scott, R. B., Richman, J. G. & Shriver, J. F. On eddy viscosity, energy cascades, and the
290 horizontal resolution of gridded satellite altimeter products. *J. Phys. Oceanogr.* **43**, 283–300 (2013).
- 291 12. Qiu, B., Chen, S., Klein, P., Sasaki, H. & Sasai, Y. Seasonal mesoscale and submesoscale eddy variability along the North
292 Pacific Subtropical Countercurrent. *J. Phys. Oceanogr.* **44**, 3079–3098 (2014).
- 293 13. Wang, S., Liu, Z. & Pang, C. Geographical distribution and anisotropy of the inverse kinetic energy cascade, and its role in
294 the eddy equilibrium processes. *J. Geophys. Res. Ocean.* **120**, 4891–4906 (2015).
- 295 14. Rhines, P. B. Waves and turbulence on a beta-plane. *J. Fluid Mech.* **69**, 417–443 (1975).
- 296 15. Capet, X., McWilliams, J. C., Molemaker, M. J. & Shchepetkin, A. Mesoscale to submesoscale transition in the California
297 Current System. Part I: Flow structure, eddy flux, and observational tests. *J. Phys. Oceanogr.* **38**, 29–43 (2008).
- 298 16. Soh, H. S. & Kim, S. Y. Diagnostic characteristics of submesoscale coastal surface currents. *J. Geophys. Res. Ocean.* **123**,
299 1838–1859 (2018).
- 300 17. Schubert, R., Gula, J., Greatbatch, R. J., Baschek, B. & Biastoch, A. The submesoscale kinetic energy cascade: Mesoscale
301 absorption of submesoscale mixed layer eddies and frontal downscale fluxes. *J. Phys. Oceanogr.* **50**, 2573–2589 (2020).
- 302 18. Balwada, D., Xie, J.-H., Marino, R. & Feraco, F. Direct observational evidence of an oceanic dual kinetic energy cascade
303 and its seasonality. *Sci. Adv.* **8**, eabq2566 (2022).

- 304 19. Garabato, A. C. N. *et al.* Kinetic energy transfers between mesoscale and submesoscale motions in the open ocean's upper
305 layers. *J. Phys. Oceanogr.* **52**, 75–97 (2022).
- 306 20. Qiu, B., Nakano, T., Chen, S. & Klein, P. Bi-Directional Energy Cascades in the Pacific Ocean From Equator to Subarctic
307 Gyre. *Geophys. Res. Lett.* **49**, e2022GL097713 (2022).
- 308 21. Leonard, A. Energy cascade in large-eddy simulations of turbulent fluid flows. In *Advances in geophysics*, vol. 18, 237–248
309 (Elsevier, 1975).
- 310 22. Germano, M. Turbulence: the filtering approach. *J. Fluid Mech.* **238**, 325–336 (1992).
- 311 23. Eyink, G. L. Locality of turbulent cascades. *Phys. D: Nonlinear Phenom.* **207**, 91–116 (2005).
- 312 24. Aluie, H., Hecht, M. & Vallis, G. K. Mapping the energy cascade in the North Atlantic Ocean: the coarse-graining
313 approach. *J. Phys. Oceanogr.* **48**, 225–244 (2018).
- 314 25. Steinberg, J. M., Cole, S. T., Drushka, K. & Abernathey, R. P. Seasonality of the Mesoscale Inverse Cascade as Inferred
315 from Global Scale-Dependent Eddy Energy Observations. *J. Phys. Oceanogr.* (2022).
- 316 26. Contreras, M., Renault, L. & Marchesiello, P. Understanding Energy Pathways in the Gulf Stream. *J. Phys. Oceanogr.*
317 (2022).
- 318 27. Srinivasan, K., Barkan, R. & McWilliams, J. C. A forward energy flux at submesoscales driven by frontogenesis. *J. Phys.*
319 *Oceanogr.* **53**, 287–305 (2023).
- 320 28. Vergara, O., Morrow, R., Pujol, M.-I., Dibarboore, G. & Ubelmann, C. Global submesoscale diagnosis using along-track
321 satellite altimetry. *Ocean. Sci.* **19**, 363–379 (2023).
- 322 29. Lahaye, N., Gula, J. & Roullet, G. Sea surface signature of internal tides. *Geophys. Res. Lett.* **46**, 3880–3890 (2019).
- 323 30. Lawrence, A. & Callies, J. Seasonality and spatial dependence of meso-and submesoscale ocean currents from along-track
324 satellite altimetry. *J. Phys. Oceanogr.* (2022).
- 325 31. Qiu, B. *et al.* Seasonality in Transition Scale from Balanced to Unbalanced Motions in the World Ocean. *J. Phys. Oceanogr.*
326 **48**, 591–605 (2018).
- 327 32. Storer, B. A., Buzzicotti, M., Khatri, H., Griffies, S. M. & Aluie, H. Global energy spectrum of the general oceanic
328 circulation. *Nat. communications* **13**, 1–9 (2022).
- 329 33. Xu, Y. & Fu, L.-L. The effects of altimeter instrument noise on the estimation of the wavenumber spectrum of sea surface
330 height. *J. Phys. Oceanogr.* **42**, 2229–2233 (2012).
- 331 34. Dufau, C., Orsztynowicz, M., Dibarboore, G., Morrow, R. & Le Traon, P.-Y. Mesoscale resolution capability of altimetry:
332 Present and future. *J. Geophys. Res. Ocean.* **121**, 4910–4927 (2016).
- 333 35. Klein, P. *et al.* Ocean-scale interactions from space. *Earth Space Sci.* **6**, 795–817 (2019).
- 334 36. Gula, J., Theetten, S., Cambon, G. & Roullet, G. Description of the GIGATL simulations (2021). URL <https://doi.org/10.5281/zenodo.4948523>. DOI 10.5281/zenodo.4948523.
- 335 37. Shchepetkin, A. & McWilliams, J. C. The Regional Oceanic Modeling System (ROMS): A split-explicit, free-surface,
336 topography-following- coordinate ocean model. *Ocean. Meteorol.* **9**, 347–404 (2005).
- 337 38. Arakawa, A. & Lamb, V. R. Computational design of the basic dynamical processes of the UCLA general circulation
338 model. *Gen. circulation models atmosphere* **17**, 173–265 (1977).
- 339 39. Carton, J. & Giese, B. A reanalysis of ocean climate using Simple Ocean Data Assimilation (SODA). *Mon. Weather. Rev.*
340 **136**, 2999–3017 (2008).
- 341 40. Renault, L., Masson, S., Arsouze, T., Madec, G. & McWilliams, J. C. Recipes for how to force oceanic model dynamics. *J.*
342 *Adv. Model. Earth Syst.* **12**, e2019MS001715 (2020).

344 Acknowledgements

345 The authors gratefully acknowledges support from the French National Agency for Research (ANR) through the project
346 DEEPER (ANR-19-CE01-0002-01). J.G. further gratefully acknowledges support from ISblue “Interdisciplinary graduate
347 school for the blue planet” (ANR-17- EURE-0015).

348 **Author contributions**

349 R.S. and J.G. designed the study. J.G. performed the numerical model simulations. O.V. computed the monthly climatology of
350 the transition scale from balanced to unbalanced flows. R.S. developed and executed all other analysis, produced the figures
351 and wrote the text. J.G. and O.V. contributed to the discussion of the results and the writing of the manuscript.

352 **Competing interests**

353 The authors declare no competing interests.

